UDC 539.4

Simulation of the Spindle Coupled Multi-Axial Loading Fatigue Test of a Rear Axle

Z. Dong,[a,1] X. Wang,[a] W. Lou,[a] Y. Huang,[b] M. Zhong,[b] H. Fan,[b] and L. Peng[b]

[a] State Key Laboratory of Automotive Safety and Energy, Department of Automotive Engineering, Tsinghua University, Beijing, China

[b] SAIC GM Wuling Automobile Co., Ltd., Liuzhou, China

[1] dongzc13@mails.tsinghua.edu.cn

УДК 539.4

Численное моделирование многоосного циклического нагружения задней оси автомобиля с учетом взаимодействия различных факторов

З. Донг[а], К. Ванг[а], В. Лоу[а], Я. Хуанг[б], М. Жонг[б], Х. Фан[б], Л. Пенг[б]

[а] Лаборатория диагностики, безопасности и энергии автомобилей, Университет Цинхуа, Пекин, Китай

[б] ООО SAIC Motor, General Motors, Liuzhou Wuling Motors Co Ltd., Лючжоу, Китай

Предложен практический метод моделирования многоосного циклического нагружения задней оси автомобиля с учетом взаимодействия различных факторов. Разработана динамичная конечноэлементная модель задней оси и выполнена ее верификация с помощью калибровочных тестов при статическом нагружении. С использованием испытательной системы Schenck ITFC моделируется процесс, включающий идентификацию системы, вычисление входных сигналов нагрузки для конечноэлементной модели, выходных сигналов напряжения и деформации, а также сравнение расчетных сигналов с реальными. С помощью программного обеспечения Matlab реализованы легко воспроизводимые программы обработки данных. Проведено измерение динамических сигналов напряжения в течение 2,441.216 с нагружения на автомобильном стенде Hainan посредством тензодатчиков, размещенных в ключевых точках задней оси автомобиля. Получено удовлетворительное согласование между расчетным и экспериментальным распределением деформации в задней оси автомобиля.

Ключевые слова: многоосное циклическое нагружение, задняя ось, метод конечных элементов, частотная функция, воспроизведение истории деформирования.

Introduction. In addition to meeting the relevant performance requirements, such as ride comfort and handling stability, the suspension mounted between the wheel and body (or frame) of the vehicle is also supposed to meet stringent strength and service-life requirements. The load affecting the tire on the ground can be decomposed into a vertical, lateral, longitudinal, and a brake force, as well as moments around corresponding axes when the vehicle is moving. The axles transmit these forces and moments to the suspension, leading to a complicated multi-axial random loading condition. The durability of the axle and suspension is mainly influenced by the vertical, lateral, longitudinal and brake force (as shown in Fig. 1), according to engineering experience. Therefore, meeting the requirements for durability and strength is one of the most significant problems to be solved during the design and development of a suspension.

In order to ensure that a suspension system can achieve the desired strength and longevity, but also to shorten the test times needed, durability tests performed in laboratories

165

have been widely applied in the worldwide automotive industry. The laboratory road test of a vehicle, which aims to replicate the conditions experienced by a vehicle in service [1–3], is a comprehensive process. Nowadays, the most realistic road durability simulators for suspensions are computer-controlled spindle coupled multi-axis loading test facilities, in which computationally intensive iterative control techniques are applied to diminish the simulation errors through an iterative process, so that the strain distribution experienced in the field can be accurately reproduced. Additionally, commercial software suites have been devised by the major servo-hydraulic test system suppliers, such as the initial release of Remote Parameter Control (RPC) by MTS in 1977 [4] and of Transfer Function Compensation (ITFC) by SCHENCK in 1979 [5]. In the late 1990's, INSTRON produced SPiDAR and LMS International developed TWR [6–8]. A spindle coupled four-axis loading simulator in which the inputs are the longitudinal force F_x, vertical force F_z, lateral force F_y, and moment about the wheel axis M_y [9, 10] is commonly used.
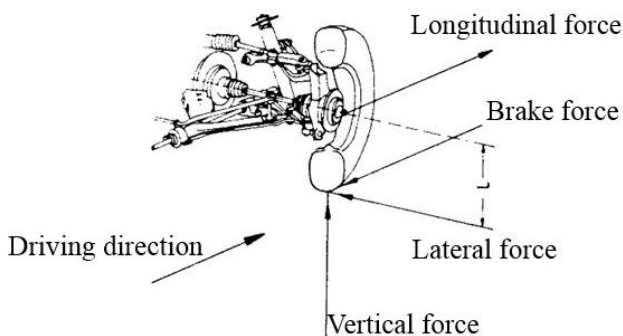

Fig. 1. Loads and forces acting on a car wheel.

Here, the theory and methodology of the ITFC algorithm by SCHENCK is introduced, which includes the following three main steps.

Step 1. **System Identification**. Figure 2 shows the principle outline of system identification. In order to identify the dynamic characteristics of the whole test system, including the test specimen, hydraulic system, filters, D/A, A/D and response-measuring system), the computer sends an identification drive signal, which is close to a white noise, to each input channel in turns, and the response signals of all channels are measured. The identification signals y_i ($i = 1, 2, \ldots, m$, where m is the total number of all input channels) in the time domain are generated by the computer. When an identification signal is sent to an input channel, the input signals to the other channels are kept at zero, with the measured response signals being x_{ij} ($i, j = 1, 2, \ldots, m$) in the time domain.
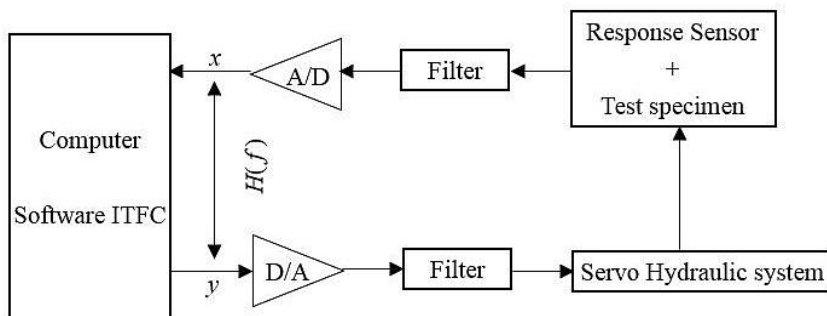

Fig. 2. Principle outline of system identification in ITFC.

The frequency response functions are calculated using the following equations:

$$H_{ij}(f) = \frac{X_{i,j}(f)}{Y_i(f)} \quad (i, j = 1, 2, ..., m), \tag{1}$$

where $X_{i,j}(f)$ is the Fourier transformation of $x_{i,j}$,

$$X_{i,j}(f) = FFT(x_{i,j}), \tag{2}$$

$Y_i(f)$ is the Fourier transformation of y_i,

$$Y_i(f) = FFT(y_i), \tag{3}$$

whereby *FFT* represents the fast Fourier transformation, f is the frequency, $H_{ij}(f)$ is the frequency response function for the input signal y_i and response signal $x_{i,j}$ caused by y_i, and m is the number of the input and output channels.

The system frequency response matrix $H(f)$ is devised as follows:

$$H(f) = [H_{ij}(f)]. \tag{4}$$

As shown in Fig. 2, one group of input signals y_i ($i = 1, 2, ..., m$) will generate one corresponding group of response signals x_i ($i = 1, 2, ..., m$), with the response signals being calculated using the formula

$$X^T(f) = Y^T(f)H(f), \tag{5}$$

where T represents matrix transposition and $X^T(f)$ is the row matrix of response signals:

$$X^T(f) = [X_1(f)X_2(f) \cdots X_m(f)], \tag{6}$$

whereby $X_i(f)$ is the Fourier transformation of the response signal x_i, and $Y^T(f)$ is the row matrix of input signals, and

$$Y^T(f) = [Y_1(f)Y_2(f) \cdots Y_m(f)], \tag{7}$$

where $Y_i(f)$ is the Fourier transformation of the input signal y_i.

The following formula can be obtained from formula (5):

$$Y^T(f) = X^T(f)H^{-1}(f), \tag{8}$$

where $H^{-1}(f)$ is the inverse matrix of the frequency response function,

$$H^{-1}(f) = [H_{ij}(f)]_{m \times m}^{-1}. \tag{9}$$

Step 2. *Determining the Input Signals through an Iterative Process*. The response signals in the time domain, which are measured on the road, are defined as the desired response signals $x_s^T(t) = [x_{s1}, x_{s2}, ..., x_{sm}]$, which must be accurately reproduced in order to make the rig tests realistic.

In step 2, the aim is to determine the input signal $y^T(t) = [y_1, y_2, ..., y_m]$, which ensures that the desired response signal $x_s^T(t) = [x_{s1}, x_{s2}, ..., x_{sm}]$ can be reproduced with acceptable accuracy. In order to improve the accuracy of this reproduction, an iterative process is applied to compensate for the non-linearity of the test system.
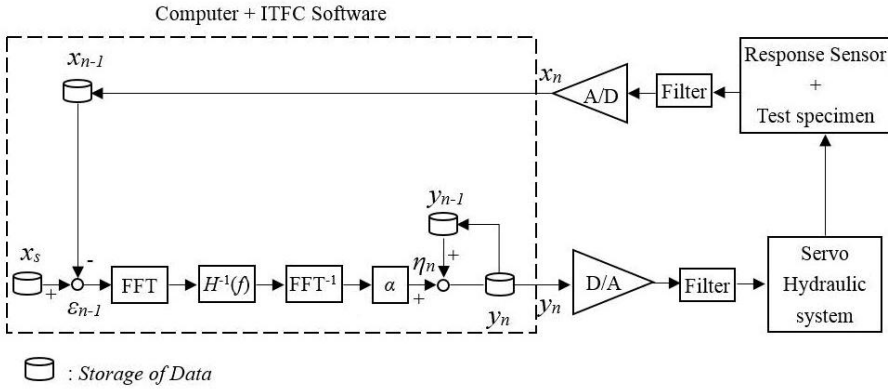

Fig. 3. Diagram of the iterative process used in the ITFC test system.

Figure 3 shows a diagrammatic representation of the iterative process for determining the input signal from the desired response signal. In Fig. 3, $x^T(t) = [x_1, x_2, ..., x_m]$ is the achieved response signal, whereas $\varepsilon^T(t) = [\varepsilon_1, \varepsilon_2, ..., \varepsilon_m]$ is the error signal between the response signal $x_s^T(t) = [x_{s1}, x_{s2}, ..., x_{sm}]$ and obtained signal $x^T(t) = [x_1, x_2, ..., x_m]$:

$$\varepsilon^T(t) = x_s^T(t) - x^T(t) = [x_{s1}, x_{s2}, ..., x_{sm}] - [x_1, x_2, ..., x_m]. \tag{10}$$

The term $\eta^T(t) = [\eta_1, \eta_2, ..., \eta_m]$ is the correcting signal, $y^T(t) = [y_1, y_2, ..., y_m]$ is the input signal, and $E^T = [E_1, E_2, ..., E_m]$ is the weighted error signal, which is calculated using the formula

$$E_i = 0.8 \frac{\int_0^t (x_{si} - x_i)^2 \, dt}{\int_0^t x_{si}^2 \, dt} + 0.2 \frac{|\varepsilon_{i\,max}|}{x_{si\,max}}. \tag{11}$$

The First Iteration Step. The aim of the first iteration is to determine the initial input signal y_1 from the desired response signal x_s. The last-step response signal $x_0(t)$ and input signal $y_0(t)$ are all zero row matrices. Thus,

$$\varepsilon_0(t) = x_s(t) - x_0(t) = x_s(t), \tag{12}$$

$$X_s(f) = FFT[x_s(t)], \tag{13}$$

$$\eta_1^T(t) = \alpha \cdot FFT^{-1}[X_s^T(f) H^{-1}(f)], \tag{14}$$

where FFT^{-1} represents the inverse fast Fourier transformation, and α is the attenuation matrix:

$$\alpha = \begin{bmatrix} \alpha_1 & & & \\ & \alpha_2 & & \\ & & \ddots & \\ & & & \alpha_m \end{bmatrix} \qquad (\alpha_i < 1,\ i = 1, 2, \ldots, m). \qquad (15)$$

Considering the non-linearity of the system, $[\alpha]$, which is a diagonal matrix, should be applied in order to avoid iteration divergence and improve the accuracy.

The input signal obtained in the first iteration step is as follows:

$$y_1^T(t) = y_0^T(t) + \eta_1^T(t) = \alpha \cdot FFT^{-1}[X_s^T(f)H^{-1}(f)]. \qquad (16)$$

Subsequently, y_1 is sent to the test system and the first achieved response x_1 is measured. The error signal between x_s and x_1, $\varepsilon_1 = x_s - x_1$, and the weighted error $E_1^T = [E_{11}, E_{12}, \ldots, E_{1m}]$ are calculated via formulas (10) and (11), respectively. Presuming that E_s is the desired weighted error, if $E_{1i} \le E_s$, the iteration will be stopped and y_1 is the driving signal needed. If, on the other hand, $E_{1i} > E_s$, the next iteration step will be conducted.

The nth Iteration. In the *n*th iteration, the *n*th input signal y_n is determined from the desired response signal x_s, the achieved response signal x_{n-1} and the input signal y_{n-1}, which are obtained in the last step:

$$\varepsilon_{n-1}(t) = x_s(t) - x_{n-1}(t), \qquad (17)$$

$$\varepsilon_{n-1}(f) = FFT[\varepsilon_{n-1}(t)], \qquad (18)$$

$$\eta_n^T(t) = \alpha \cdot FFT^{-1}[\varepsilon_{n-1}^T(f)H^{-1}(f)], \qquad (19)$$

$$y_n^T(t) = y_{n-1}^T(t) + \eta_n^T(t). \qquad (20)$$

After this, y_n is sent to the test system and the achieved response x_n is measured. The error signal between x_s and x_n, $\varepsilon_n = x_s - x_n$, and the weighted error signal $E_n^T = = [E_{n1}, E_{n2}, \ldots, E_{nm}]$ are again calculated using the formulas (10) and (11), respectively. If $E_{ni} \le E_s$, the iteration process will be stopped, with y_n being the input signal needed. If $E_{1i} > E_s$, the next iteration step will be conducted, until the weighted errors converge to an acceptable tolerance level.

Step 3. Performing the Durability Test. Figure 4 shows a diagrammatic representation of the durability test. The test system operates in an open-loop control mode, whereby the final input signal $y_n(t)$, obtained at the end of the above iteration process, is repeatedly sent to the test system until the test specimen is broken or the requirement for durability is fulfilled. In such a test, the strain distribution in the specimen experienced on the road can be accurately reproduced, yielding realistic test results.

In recent years, many vehicle manufacturers are moving towards virtual test simulations instead of the laboratory or proving ground tests, because they need to shorten the development period of new product and reduce costs in the competitive market environment. At the time of writing, there are two main virtual test simulation methods: the virtual proving ground (VPG) and virtual test rig (VTR) [11–14]. Their main advantage lies in the fact that the quality of the design can be evaluated even before a prototype is available [15].
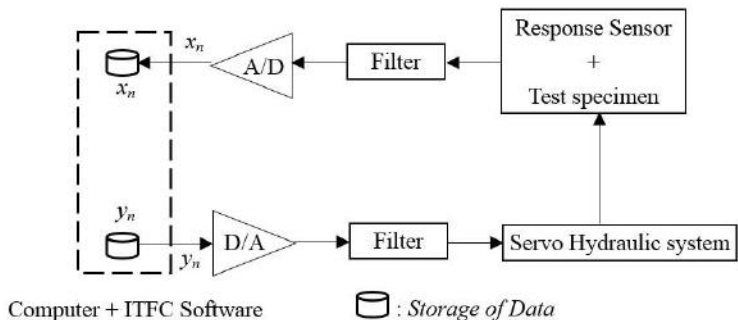
Fig. 4. Diagrammatic representation of the durability test.

The methodology of VPG is as follows: (i) building a geometry model of the test tracks of the proving ground [13, 14]; (ii) building a finite element model of the whole vehicle including a tire model [13]; (iii) simulation of the vehicle driving on the proving ground and calculation of the strain, stress and acceleration response histories; (iv) calculation of longevity and fatigue damage. However, the VPG technology imposes truly vast demands on computer resources. The time period and corresponding road length which can be simulated within the limits of available computer resources and calculating time is thus quite short, and consequently cannot represent the test on the proving ground with sufficiently high statistical significance.

VTR technology is mainly used to evaluate the durability of the vehicle's body or frame. Figure 5 shows a typical virtual four-poster test rig model with four vertical displacements as inputs [9]. The VTR methodology is as follows: (i) building a model of the actuators [9]; (ii) building a finite element model of the whole vehicle including a tire model [13]; (iii) simulating the vehicle driving on the proving ground with the control signals being the acceleration signals measured on the proving ground, or with the geometry model of the test tracks of the proving ground as the input signals and calculating the strain, stress and acceleration response histories; (iv) calculating the vehicle's life and fatigue damage. The limitations of such VTR technology are similar, in principle, to those encountered with VPG [16–18].
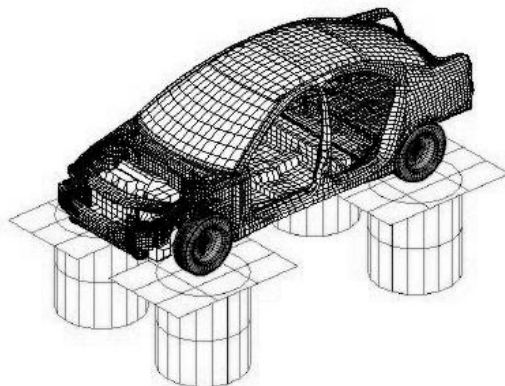

Fig. 5. A virtual four-poster test rig model [19].

This paper aims to establish a simplified virtual test rig method which can accurately reproduce the strain distribution in a selected specimen, thus avoiding the problems associated with constructing a complicated finite-element model of the whole vehicle, including the tire, and consequently prolonging the time interval, which can be simulated.
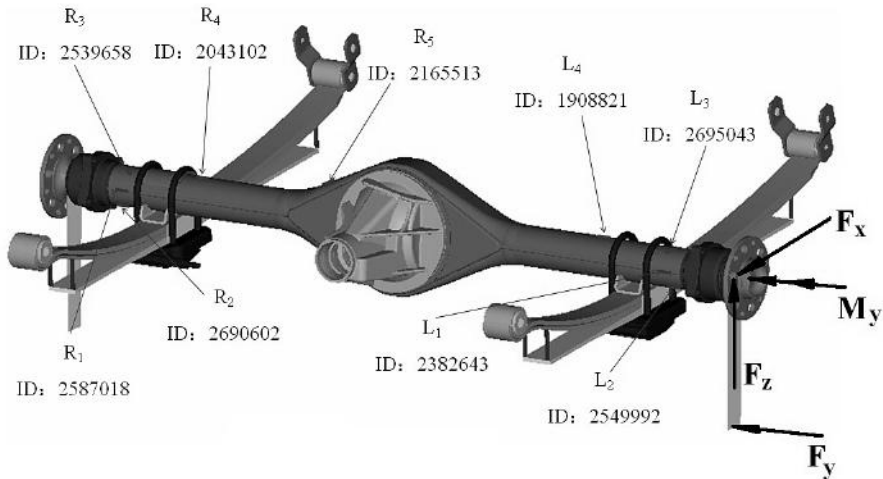
Fig. 6. A model of the mini-bus rear axle used as specimen in this study.

The mini-bus rear axle illustrated in Fig. 6 was selected as the specimen. A virtual rig test or spindle coupled four-axial loading rig test based on the theory and methodology of ITFC were simulated using the strain signals of the strain gauges L_i and R_i ($i = 1, 2, 3, 4$) measured on the Hainan proving ground according to the specifications of the SAIC GM Wuling Automobile Co., Ltd. (SGMW, for short) durability test. We used the desired response signals, together with the vertical force F_z, lateral force F_y, longitudinal force F_x, and moment M_y of both sides of the axle as inputs.

1. **Simulation of the Spindle Coupled Multi-Axial Loading Rig Test of the Rear Axle**. The simulation of the spindle coupled multi-axial loading rig test of the rear axle is based on ITFC methodology. The first step comprised system identification, and Fig. 7 shows a flowchart of this process. A dynamic finite-element model of the rear axle was used in place of the real, physical axle, servo-hydraulic loading system and signal measurement system. A program for calculating the identification input forces and moments was compiled, with which the input signals and the response stress signals were calculated based on this finite-element model. The strain signals, on the other hand, were calculated
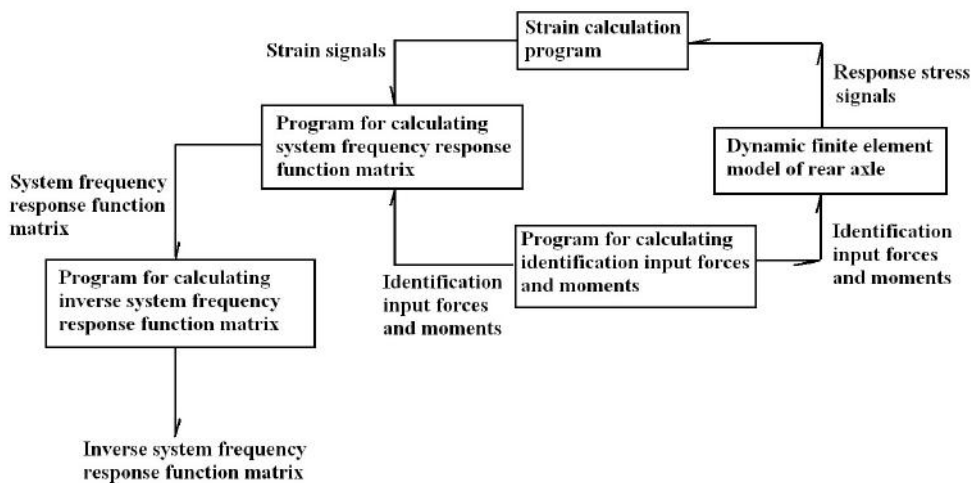

Fig. 7. Flowchart of the system identification process.

from the response stress signals, using a strain calculation program. The strain, input force and moment signals were then used to calculate the system frequency response function matrix. Finally, an inverse system frequency function matrix was obtained. All calculation programs were compiled in Matlab.

In another step, the input force and moment signals, used to reproduce the proving ground strain signals, were determined (see Fig. 8 for a flowchart). The dynamic finite-element model of the rear axle was again applied in place of the real axle, servo-hydraulic loading system and signal measurement system.
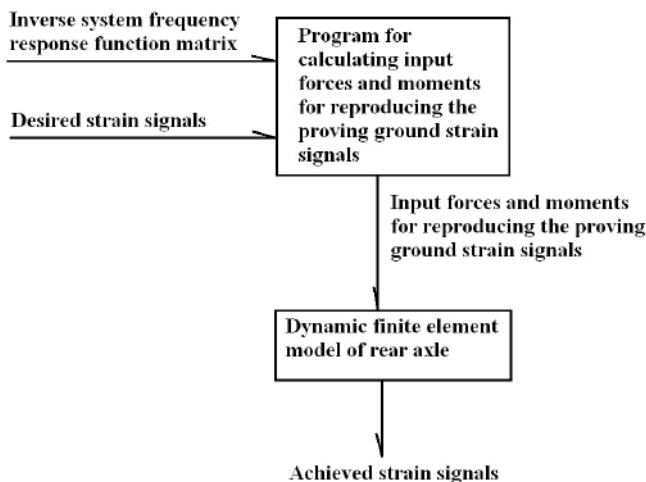

Fig. 8. Flowchart for determining the input force and moment signals used to reproduce the proving ground strain signals.

In a final step, the stress signals of critical points or elements of the rear axle finite-element model were obtained and processed to predict their fatigue damage and longevity using software based on the local stress-strain theory.

2. **Finite-Element Model of the Rear Axle**. The dynamic finite-element model is the key for a successful simulation of the spindle coupled multi-axis loading test of the rear axle, and thus must be properly constructed. The model, illustrated in Fig. 9, was constructed and analyzed using Altair HyperWorks 12.0 (Altair Engineering, Inc.). The rear axle was modeled using solid elements (CTETRA) and shell elements (CTRIA3), with dimensions ranging from 2 to 5 mm. Revolving joints were simulated using RBE2. Since the axle housing is the focus of this study, the dimensions of the elements for modeling this component, encompassing the upper and bottom housing carriers, were 2 mm, while the dimensions of the elements for all other components were 5 mm. Table 1 lists the types, dimensions and thicknesses of the elements used to model each component.

The axle shafts were modeled using the solid CTETRA elements, with element dimensions of approximately 5 mm. The outboard bearings of the axle shaft, bearing the largest forces, were also modeled using the solid CTETRA elements, which dimensions of 5 mm, as shown in Fig. 9b. The inboard bearings of the axle shafts, which bear much smaller forces than the outboard ones, were modeled using the CTRIA3 plate and shell elements, and their dimensions and thicknesses are given in Table 1 and shown in Fig. 9c.

The leaf springs were simplified as linear, by building leaf-end links and leaf-mid links between the three leaf springs, as shown in Fig. 9a, d, and e. This models the leaf spring in its fully loaded state. In order to obtain the correct stiffness of the leaf spring, a group of virtual material properties was selected, with the virtual elastic modulus $E = 100$ GPa, Poisson's ratio $\mu = 0.3$, and density $\rho = 7900$ kg/m^3. This treatment was
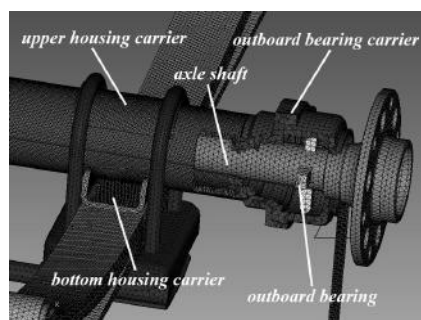
T a b l e 1

Types, Dimensions, and Thicknesses of the Elements Used to Model the Components of the Rear Axle

Component	Element type	Element dimension (mm)	Element thickness (mm)
Loading bar	CTRIA3	5	50
Leaf-end link	CTRIA3	5	1
Leaf-mid link	CTRIA3	5	5
Inboard bearings	CTRIA3	5	2
Revolving joints	RBE2	–	–
Housing	CTETRA	2	–
Axle carrier	CTETRA	2	–
Upper housing carrier	CTETRA	2	–
Bottom housing carrier	CTETRA	2	–
Axle shaft	CTETRA	5	–
Outboard bearing carrier	CTETRA	5	–
Outboard bearing	CTETRA	5	–
Rubber bushing	CTETRA	5	–
Lifting lug	CTETRA	5	–
U bolt	CTETRA	5	–

a

b

c

d

e   f
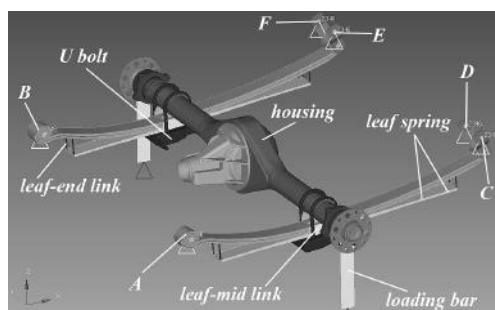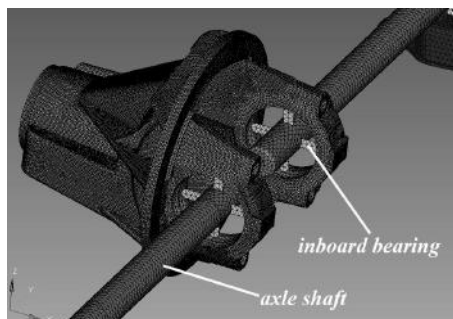
Fig. 9. Details of the dynamic-finite element model of the rear axle.

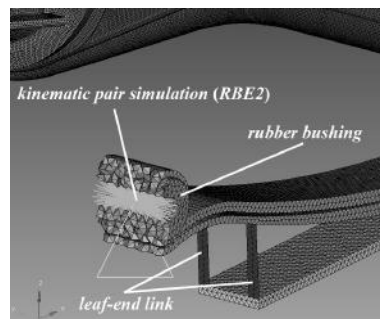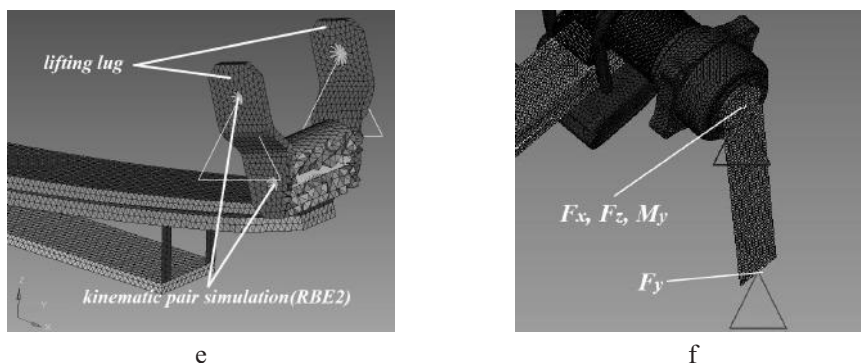chosen because it is beneficial for calculation speed. The types, dimensions and thicknesses of the elements used for the leaf-end and leaf-mid links are also listed in Table 1.

Rubber bushings (as shown in Fig. 9d and e) were used to connect the steel components in the model, and it was assumed that the deformation of each rubber bushing is small and that their material properties could be approached by a virtual elastic material with an elastic modulus of $E = 1$ MPa, Poisson's ratio $\mu = 0.48$, and density $\rho = 1650$ kg/m^3, which again was beneficial for calculation speed.

The axle carrier is made of cast iron, and the material properties of the elements used to model it were thus as follows: elastic modulus $E = 170$ GPa, Poisson's ratio $\mu = 0.25$, and density $\rho = 7900$ kg/m^3. The material properties of the elements for modeling other axle components were as follows: elastic modulus $E = 203$ GPa, Poisson's ratio $\mu = 0.3$, and density $\rho = 7900$ kg/m^3.

The rotating centers of the front and rear lifting-lugs were modeled using nodes A, B, C, D, E, and F, as shown in Fig. 9a, and their translational degrees of freedom along the X, Y, and Z axes and the rotational degrees of freedom around these axes were restrained. Therefore, only rotation around the Y axis was allowed. The revolving joints were also simulated in this way.

The loading bars simulating the tires were modeled using CTRIA3 shell elements with dimensions of 5 mm and a thickness of 50 mm. The distance between the left and right loading bars corresponded to the track width of 1480 mm. The vertical length of the loading bar was equal to the tire radius of 305 mm, as shown in Fig. 9a. F_Y was applied on the lower center point of the loading bar, whereas F_Z, F_X, and M_Y were all applied on the axle shaft center point, as shown in Fig. 9f.

Thus, the dynamic finite-element model used in this study is a fully linear one. In order to confirm its accuracy, a static calibration test was performed using the test system shown in Fig. 10. Seven strain gauges (L_1, L_2, L_4, R_1, R_2, R_4, and R_5) and two 45° rosettes (L_3 and R_3) were attached to the surface of the axle housing, as shown in Fig. 11. The corresponding element ID numbers are L_1–L_4 and R_1–R_4, as shown in Fig. 6. The strain gauges L_1, L_2, L_4, R_1, R_2, R_4, and R_5 were used to measure the strains in the Y direction, whereas L_3 and R_3 were used to measure the strains at an angle of 45° to Y. L_1 and R_1 measured the longitudinal force F_X, whereas L_2, L_4, R_2, and R_4 were sensitive to the vertical force F_Z and lateral force F_Y. L_3 and R_3 reacted to the brake force F_B, as shown in Fig. 10.

The static calibration test was performed under four loading conditions: (i) only vertical force F_Z is applied; (ii) lateral force F_Y and vertical force F_Z are applied; (iii) longitudinal force F_X and vertical force F_Z are applied; (iv) brake force F_B and

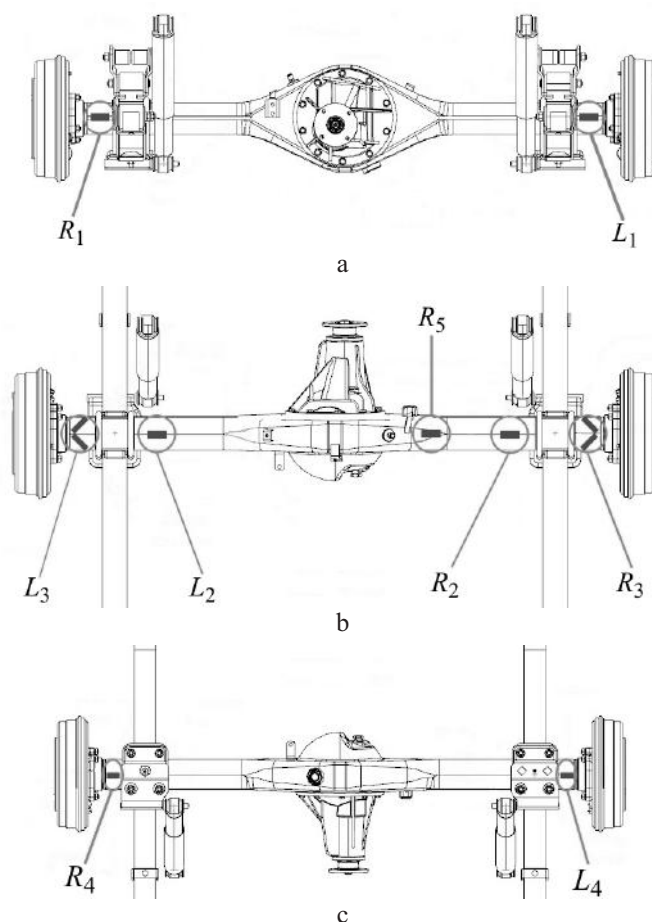Fig. 10. Static calibration test system.

Fig. 11. Positions of strain gauges attached to the surface of the axle housing: (a) front view; (b) top view; (c) bottom view.

vertical force F_Z are applied. The strain signals were measured using the strain gauges and rosettes placed in the positions shown in Fig. 11.

In order to check the accuracy of the dynamic finite element model shown in Fig. 9, a corresponding static model was constructed, which was basically the same as the dynamic one except for the input forces and moments. Figure 12 shows the input forces of the static element model including the vertical force F_Z, lateral force F_Y, longitudinal force F_X, and brake force F_B.
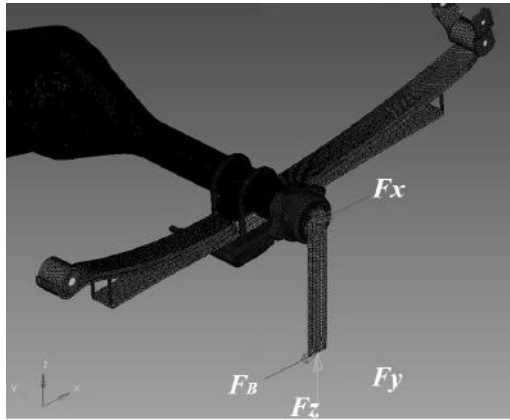

Fig. 12. Input forces of the static finite-element model of the rear axle.

The stress distribution of the rear axle under each load condition was calculated using the static finite-element model. The RADIOSS module of Altair HyperWorks 12.0 was used to perform the model analysis. The normal Y strain ε_{yc}, which corresponds to that measured using the strain gauges L_1, L_2, L_4, R_1, R_2, R_4, or R_5 was calculated using formula (21):

$$\varepsilon_{yc} = \frac{1}{E}[\sigma_y - \mu(\sigma_x + \sigma_z)], \tag{21}$$

where σ_x, σ_y, and σ_z represent the calculated normal *X*, *Y*, and *Z* stresses of the element on which the corresponding strain gauge is placed. Presuming the strain ε_T is the strain measured with the rosette L_3 or R_3, then

$$\varepsilon_T = \frac{1}{2}(\varepsilon_{45} - \varepsilon_{135}), \tag{22}$$

whereby ε_{45} and ε_{135} are the strains measured by the two strain gauges in the direction with an angle of 45° to *Y* in the strain rosette, respectively. The strains corresponding to ε_{45} and ε_{135} were calculated using formulas (23) and (24), respectively:

$$\varepsilon_{45,c} = \frac{1}{E}\left[\frac{\sigma_x + \sigma_y}{2} - \tau_{xy} - \mu\left(\frac{\sigma_x + \sigma_y + 2\sigma_z}{2} + \tau_{xy}\right)\right], \tag{23}$$

$$\varepsilon_{135,c} = \frac{1}{E}\left[\frac{\sigma_x + \sigma_y}{2} + \tau_{xy} - \mu\left(\frac{\sigma_x + \sigma_y + 2\sigma_z}{2} - \tau_{xy}\right)\right], \tag{24}$$

where $\varepsilon_{45,c}$ and $\varepsilon_{135,c}$ are the calculated strains corresponding to ε_{45} and ε_{135}, respectively, σ_x, σ_y, and σ_z are the calculated normal *X*, *Y*, and *Z* stresses of the element

on which the corresponding strain rosette is placed, respectively, and τ_{xy} is the calculated shear stress of the element. The strain ε_{Tc}, which corresponds to ε_T is calculated using formula (25):

$$\varepsilon_{Tc} = \frac{1}{2}(\varepsilon_{45,c} - \varepsilon_{135,c}) = -\frac{\tau_{xy}}{E}(1+\mu). \tag{25}$$

Tables 2–5 show a comparison between the strains measured in the static calibration test and the corresponding strains calculated using the formulas (21), (23), (24), and (25), with the error calculated using formula (26):

$$Error = \frac{|S_c - S_m|}{S_m} \cdot 100\%, \tag{26}$$

where *Error* is the relative error between the measured strain S_m and the corresponding calculated strain S_c. As can be seen in these tables, one error was 24.11% which is the error corresponding to the strain gauge L_1 under the loading condition in which a longitudinal and a vertical force are applied, with the remaining errors all being smaller than 16%. Thus, the accuracy of the finite-element model of the rear axle is acceptable.

T a b l e 2
**Comparison of Strains Measured and Calculated for the Loading Condition
in which only a Vertical Force $F_Z = 5000$ N is Applied**

	L_1	R_1	L_2	R_2	L_3	R_3	L_4	R_4
S_m ($\mu\varepsilon$)	–	–	171.094	135.395	–	–	−219.090	−180.835
S_c ($\mu\varepsilon$)	–	–	153.655	152.201	–	–	−185.069	−186.535
Error	–	–	10.19%	12.41%	–	–	15.53%	3.15%

T a b l e 3
**Comparison of Strains Measured and Calculated for the Loading Condition
in which a Lateral Force $F_Y = 5000$ N and Vertical Force $F_Z = 5000$ N are Applied**

	L_1	R_1	L_2	R_2	L_3	R_3	L_4	R_4
S_m ($\mu\varepsilon$)	–	–	−215.863	−205.371	–	–	195.042	175.021
S_c ($\mu\varepsilon$)	–	–	−230.586	−228.246	–	–	202.132	202.605
Error	–	–	6.82%	11.14%	–	–	3.63%	15.76%

T a b l e 4
**Comparison of Strains Measured and Calculated for the Loading Condition
in which a Longitudinal Force $F_X = 5000$ N and Vertical Force $F_Z = 5000$ N are Applied**

	L_1	R_1	L_2	R_2	L_3	R_3	L_4	R_4
S_m ($\mu\varepsilon$)	−113.841	−125.714	–	–	–	–	–	–
S_c ($\mu\varepsilon$)	−141.283	−144.517	–	–	–	–	–	–
Error	24.11%	14.96%	–	–	–	–	–	–

T a b l e 5

Comparison of Strains Measured and Calculated for the Loading Condition in which the Brake Force $F_B = 3000$ N and Vertical Force $F_Z = 5000$ N are Applied

	L_1	R_1	L_2	R_2	L_3	R_3	L_4	R_4
$S_m (\mu\varepsilon)$	–	–	–	–	111.740	111.740		
$S_c (\mu\varepsilon)$	–	–	–	–	116.431	110.184		
Error	–	–	–	–	4.20%	1.39%		

3. **Measurement of Rear Axle Strain Signals on the Hainan Proving Ground**. To obtain the desired response signals for the virtual laboratory simulation, the strain signals of the strain gauges L_1, L_2, L_4, R_1, R_2, R_4, and R_5, as well as the strain rosettes L_3 and R_3 (Figs. 6 and 11) of the rear axle were measured on the Hainan proving ground, according to the specifications of the SGMW durability test. The signal of R_5 was used to verify the strain distribution of the rear axle, which will be discussed later, with other measured strain signals used as the desired response signals. Figure 13 shows the measured strain time history of the strain gauges L_1 and R_1 in a full test-drive cycle, at a sampling frequency of 500 Hz, a low-pass filter cut-off frequency of 50 Hz and a duration of 2,441.216 s (1220,608 data points).
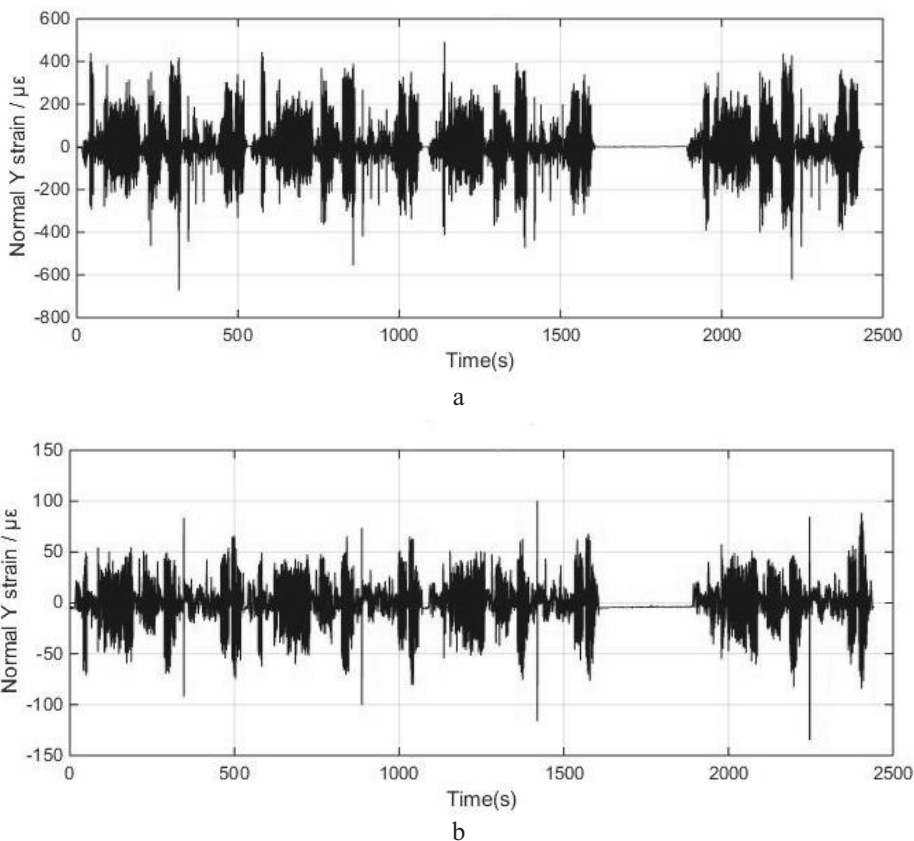

a

b

Fig. 13. Normal *Y* strain histories of the strain gauges L_1 (a) and R_1 (b) measured in a full test cycle on the Hainan proving ground according to the specifications of the SGMW durability test.

4. **System Identification**. In order to obtain the input forces and moments for the dynamic finite-element model of the rear axle, starting from the desired response signals, it was necessary to identify the system frequency response function matrix. The input forces and moments used in the dynamic finite element model of the rear axle include (1) the left vertical force F_{Z1}, lateral force F_{Y1}, longitudinal force F_{X1}, and moment M_{Y1}; and (2) the right vertical force F_{Z2}, lateral force F_{Y2}, longitudinal force F_{X2}, and moment M_{Y2}. The output signals of the dynamic finite-element model are the stresses σ_x, σ_y, σ_z, and τ_{xy} of each strain gauge, with the formula (21) used to calculate the corresponding normal Y strain ε_{yc} and formulas (23), (24), and (25) used to calculate the strain ε_{Tc} corresponding to the strain signals measured by the strain rosettes L_3 and R_4. In accordance with formula (5), this yields the following formula:

$$X_\varepsilon^T(t) = Y_{in}^T(t)[H(t)]_{8\times8}, \tag{27}$$

$$X_\varepsilon^T(t) = [x_{\varepsilon1} \quad x_{\varepsilon2} \quad x_{\varepsilon3} \quad x_{\varepsilon4} \quad x_{\varepsilon5} \quad x_{\varepsilon6} \quad x_{\varepsilon7} \quad x_{\varepsilon8}] =$$

$$= [\varepsilon_{L2} \quad \varepsilon_{R2} \quad \varepsilon_{L4} \quad \varepsilon_{R4} \quad \varepsilon_{L1} \quad \varepsilon_{R1} \quad \varepsilon_{TL} \quad \varepsilon_{TR}], \tag{28}$$

$$\varepsilon_{L2} = \frac{1}{E}[\sigma_{y,L2} - \mu(\sigma_{x,L2} + \sigma_{z,L2})], \tag{29}$$

$$\varepsilon_{R2} = \frac{1}{E}[\sigma_{y,R2} - \mu(\sigma_{x,R2} + \sigma_{z,R2})], \tag{30}$$

$$\varepsilon_{L4} = \frac{1}{E}[\sigma_{y,L4} - \mu(\sigma_{x,L4} + \sigma_{z,L4})], \tag{31}$$

$$\varepsilon_{R4} = \frac{1}{E}[\sigma_{y,R4} - \mu(\sigma_{x,R4} + \sigma_{z,R4})], \tag{32}$$

$$\varepsilon_{L1} = \frac{1}{E}[\sigma_{y,L1} - \mu(\sigma_{x,L1} + \sigma_{z,L1})], \tag{33}$$

$$\varepsilon_{R1} = \frac{1}{E}[\sigma_{y,R1} - \mu(\sigma_{x,R1} + \sigma_{z,R1})], \tag{34}$$

$$\varepsilon_{TL} = -\frac{\tau_{xy,L3}}{E}(1+\mu), \tag{35}$$

$$\varepsilon_{TR} = -\frac{\tau_{xy,R3}}{E}(1+\mu), \tag{36}$$

$$Y_{in}^T(t) = [y_{in,1} \quad y_{in,2} \quad y_{in,3} \quad y_{in,4} \quad y_{in,5} \quad y_{in,6} \quad y_{in,7} \quad y_{in,8}] =$$

$$= [F_{Z1} \quad F_{Z2} \quad F_{Y1} \quad F_{Y2} \quad F_{X1} \quad F_{X2} \quad M_{Y1} \quad M_{Y2}], \tag{37}$$

wherein $[H(t)]_{8\times8}$ is the system strain-force relationship matrix, T represents matrix transposition, $X_\varepsilon^T(t)$ is the response strain row matrix, $x_{\varepsilon j}$ ($j = 1, 2, \ldots, 8$) are the

elements of $X_\varepsilon^T(t)$, and ε_{L1}, ε_{L2}, ε_{L4}, ε_{R1}, ε_{R2}, and ε_{R4} are the calculated normal Y strains of the elements whose positions correspond to the strain gauges L_1, L_2, L_4, R_1, R_2, and R_4 (as shown in Figs. 6 and 11), respectively. The terms $\sigma_{y,L1}$, $\sigma_{x,L1}$, and $\sigma_{z,L1}$ stand for the calculated normal stresses of the element corresponding to strain L_1, with L_2 and L_4, as well as R_1, R_2, and R_4 substituted in a similar manner for the others. ε_{TL} and ε_{TR} are the calculated normal strains of the elements whose positions correspond to the strain rosettes L_3 and R_3 (as shown in Figs. 6 and 11), respectively, with $\tau_{xy,L3}$ and $\tau_{xy,R3}$ being the calculated shear stresses corresponding to the strain rosettes L_3 and R_3. $Y_{in}^T(t)$ represents the input forces and moments given as a row matrix, and $y_{in,i}$ ($i=1, 2, \dots, 8$) are the elements of $Y_{in}^T(t)$. As shown in Fig. 14, F_{Z1}, F_{X1}, F_{Y1}, and M_{Y1} are the forces and the moment applied on the left end of the rear axle, whereas F_{Z2}, F_{X2}, F_{Y2}, and M_{Y2} are the forces and the moment applied on the right end of the rear axle. The stresses mentioned above are all calculated using the dynamic finite element model of the rear axle, with the above-mentioned input forces and moments used as the inputs to the model. The dynamic finite element model was analyzed in Altair HyperWorks 12.0, using the modal transient analysis module from RADIOSS.
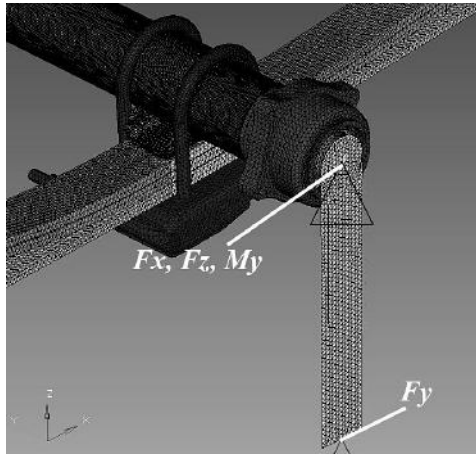

Fig. 14. Input forces and moment on the left end of the finite element model of the rear axle.

In order to calculate the system frequency response-function matrix it was first necessary to calculate the identification signal. The identification signal used here is a kind of impulse signal called pseudo impulse, the expression of which can be described with the following formula:

$$S_{pT}(t) = \frac{A_{pp}}{N} \sum_{n=n_1}^{n_2} \cos(2\pi f_n t), \tag{38}$$

$$f_n = \frac{n}{T}, \tag{39}$$

$$T = \frac{N_{FFT}}{f_s}, \tag{40}$$

$$N = n_2 - n_1 + 1, \qquad n_2 \geq n_1 \geq 0, \tag{41}$$

where $S_{pT}(t)$ is the sampling value of the pseudoimpulse signal, A_{pp} is the amplitude ($A_{pp} = 400$), N_{FFT} is the N of a N-point FFT ($N_{FFT} = 8192$), f_s is the sampling frequency ($f_s = 500$ Hz), T is the duration of the identification signal, $T = N_{FFT}/f_s = 8192/500 = 16.384$ s, f_n is the frequency at which a sampling value is calculated, n_1 is the first value of n, $n_1 = 1$, n_2 is the last value of n, $n_2 = 200$, and N is the total number of f_n. Figure 15a shows the time history of the calculated identification signal.
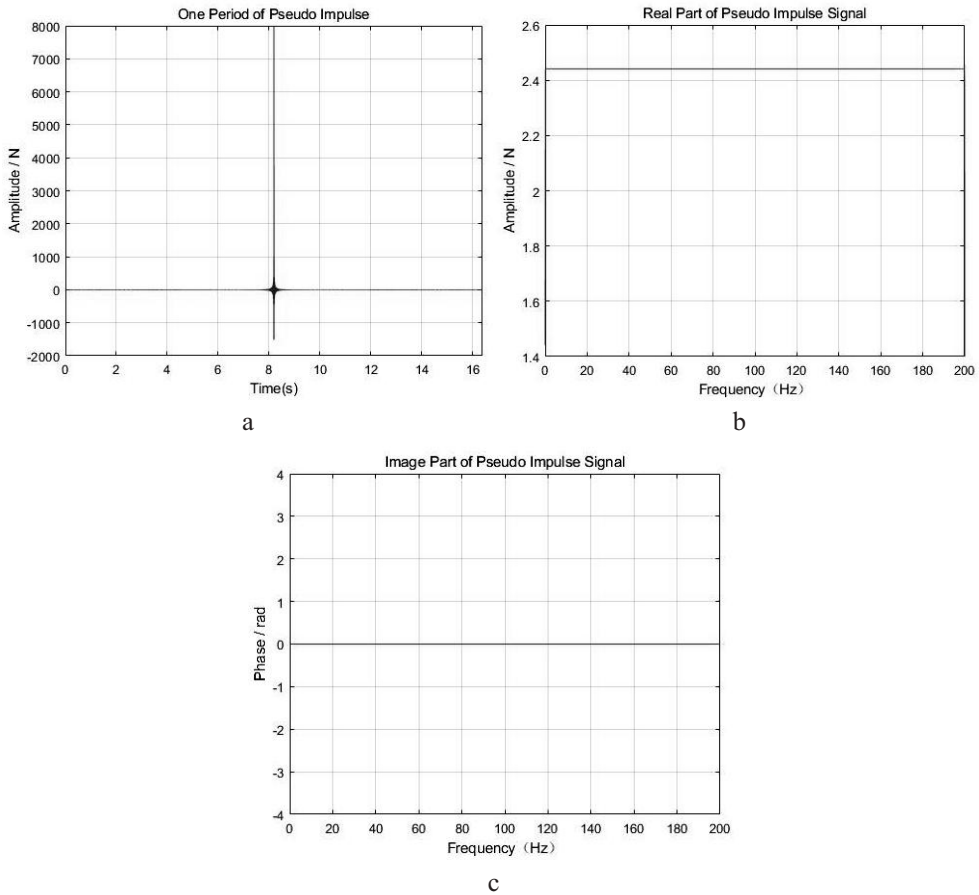

a

b

c

Fig. 15. Pseudo impulse signal and spectrum of the pseudo impulse signal.

The reason why the pseudo impulse signal is used as the system identification signal is that it has good characteristics, with its corresponding real part of the frequency spectrum being a horizontal line, and its phase also being a horizontal line corresponding to a value of zero, as shown in Fig. 15b and c. In this way, good system identification results can be obtained.

Subsequently, the stress response signals were calculated using the dynamic finite element model of the rear axle. Taking the calculated pseudo impulse signal as the signal of the ith element $y_{in,i}$ of the row matrix $Y_{in}^T(t)$ [formula (37)], with other elements in $Y_{in}^T(t)$ kept at zero, the stress response signals of the elements in the dynamic finite-element model which correspond to the strain gauges and rosettes L_1–L_4 and R_1–R_4 (Fig. 6), were calculated using the model. Figure 16 shows the time histories of σ_x, σ_y, σ_z, and τ_{xy} for each of these elements. The ID numbers of the elements were 2382,643,
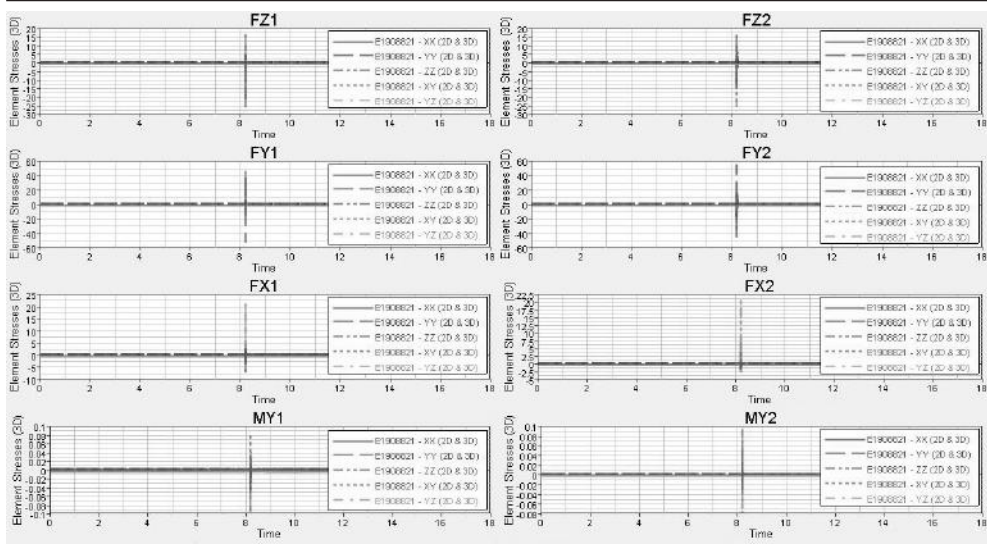
Fig. 16. Time histories of σ_x, σ_y, σ_z, and τ_{xy} of the eight elements, caused by each input force or moment.

2549,992, 2695,043, 1908,821, 2587,018, 2690,602, 2539,658, and 2043,102. The elements $x_{\varepsilon j,i}$ $(j, i = 1, 2, \ldots, 8)$ of the row matrix $X_\varepsilon^T(t)$ [formula (28)] were calculated using formulas (28)–(36), with $x_{\varepsilon j,i}$ $(j = 1, 2, \ldots, 8)$ being exclusively caused by $y_{in,i}$.

The system frequency response function matrix was also calculated. From formulas (27), (28), and (37), the formulas (42), (43), and (44) were obtained as follows:

$$X_\varepsilon^T(f) = Y_{in}^T(f)[H(f)]_{8\times8}, \tag{42}$$

$$X_\varepsilon^T(f) = [X_{\varepsilon 1} \quad X_{\varepsilon 2} \quad X_{\varepsilon 3} \quad X_{\varepsilon 4} \quad X_{\varepsilon 5} \quad X_{\varepsilon 6} \quad X_{\varepsilon 7} \quad X_{\varepsilon 8}]^T, \tag{43}$$

$$Y_{in}^T(f) = [Y_{in,1} \quad Y_{in,2} \quad Y_{in,3} \quad Y_{in,4} \quad Y_{in,5} \quad Y_{in,6} \quad Y_{in,7} \quad Y_{in,8}]^T, \tag{44}$$

where $X_\varepsilon^T(f)$ and $Y_{in}^T(f)$ are the Fourier transformations of $X_\varepsilon^T(t)$ and $Y_{in}^T(t)$, respectively, $X_{\varepsilon j}$ $(j = 1, 2, \ldots, 8)$ and $Y_{in,i}$ $(i = 1, 2, \ldots, 8)$ are the transformations of $x_{\varepsilon j}$ $(j = 1, 2, \ldots, 8)$ in formula (28) and $y_{in,i}$ $(i = 1, 2, \ldots, 8)$ in formula (37), respectively, $[H(f)]_{8\times8}$ is the system frequency response function matrix:

$$[H(f)]_{8\times8} = \begin{bmatrix} H_{11} & H_{12} & H_{13} & H_{14} & H_{15} & H_{16} & H_{17} & H_{18} \\ H_{21} & H_{22} & H_{23} & H_{24} & H_{25} & H_{26} & H_{27} & H_{28} \\ H_{31} & H_{32} & H_{33} & H_{34} & H_{35} & H_{36} & H_{37} & H_{38} \\ H_{41} & H_{42} & H_{43} & H_{44} & H_{45} & H_{46} & H_{47} & H_{48} \\ H_{51} & H_{52} & H_{53} & H_{54} & H_{55} & H_{56} & H_{57} & H_{58} \\ H_{61} & H_{62} & H_{63} & H_{64} & H_{65} & H_{66} & H_{67} & H_{68} \\ H_{71} & H_{72} & H_{73} & H_{74} & H_{75} & H_{76} & H_{77} & H_{78} \\ H_{81} & H_{82} & H_{83} & H_{84} & H_{85} & H_{86} & H_{87} & H_{88} \end{bmatrix}, \tag{45}$$

$$H_{ij} = \frac{X_{w\varepsilon j,\,i}}{Y_{win,\,i}} \qquad (i,\,j = 1,\,2,\,...,\,8), \tag{46}$$

where $X_{w\varepsilon j,\,i}$ and $Y_{win,\,i}$ are the Fourier transformations of $x_{w\varepsilon j,\,i}$ and $y_{win,\,i}$ in the time domain:

$$x_{w\varepsilon j,\,i}(n) = x_{\varepsilon j,\,i}(n) \cdot S_{st}(n), \tag{47}$$

$$y_{win,\,i}(n) = y_{in,\,i}(n) \cdot S_{st}(n), \tag{48}$$

$$S_{st}(n) = \frac{1}{1 + A_w}\left[1 - A_w \cos\left(\frac{2\pi n}{f_s T}\right)\right], \tag{49}$$

$$X_{w\varepsilon j,\,i}(f_n) = (1 + A_w)e^{j\pi n} \cdot FFT(x_{w\varepsilon j,\,i}), \tag{50}$$

$$Y_{win,\,i}(f_n) = (1 + A_w)e^{j\pi n} \cdot FFT(y_{win,\,i}), \tag{51}$$

$$f_n = \frac{n-1}{N} f_s, \qquad n = 1,\,2,\,...,\,N. \tag{52}$$

Herein, *FFT* represents the fast Fourier transformation, $x_{\varepsilon j,\,i}(n)$ and $y_{\varepsilon j,\,i}(n)$ are the *n*th sampling values of $x_{\varepsilon j,\,i}$ and $y_{in,\,i}$, $n = 1,\,2,\,...,\,N$ (*N* is the total number of the sampling values of the identification signal), $S_{st}(n)$ is the lift window function or Hanning window function for the case that $A_w = 1$ is accepted, *T* is the duration of the identification signal, f_s is the sampling frequency, and f_n is the frequency with which the sampling value of the Fourier transformation is calculated. As an example, the real and image parts of H_{11} are shown in Fig. 17.
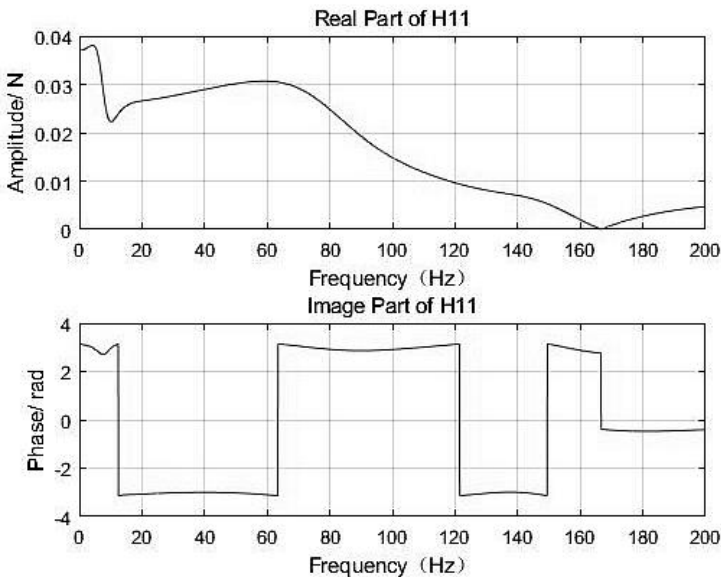

Fig. 17. Real and imaginary part of H_{11}.

5. **Calculating the Input Forces and Moments to Reproduce the Desired Strain Response Signals**. According to formulas (47)–(52), the desired signals were transferred from the time domain to the frequency domain via formulas (53)–(57):

$$x_{s,\varepsilon}^T(n) = [x_{s,\varepsilon 1}, x_{s,\varepsilon 2}, x_{s,\varepsilon 3}, x_{s,\varepsilon 4}, x_{s,\varepsilon 5}, x_{s,\varepsilon 6}, x_{s,\varepsilon 7}, x_{s,\varepsilon 8}]^T =$$

$$= [\varepsilon_{s,L2}, \varepsilon_{s,R2}, \varepsilon_{s,L4}, \varepsilon_{s,R4}, \varepsilon_{s,L1}, \varepsilon_{s,R1}, \varepsilon_{s,TL}, \varepsilon_{s,TR}]^T, \tag{53}$$

$$x_{ws,\varepsilon}^T(n) = x_{s,\varepsilon}^T(n) \cdot S_{st}(n), \tag{54}$$

$$X_{s,\varepsilon}^T(f_n) = (1 + A_w)e^{j\pi n} \cdot FFT(x_{ws,\varepsilon}^T), \tag{55}$$

$$X_{s,\varepsilon}^T(f_n) = [X_{s,\varepsilon 1}, X_{s,\varepsilon 2}, X_{s,\varepsilon 3}, X_{s,\varepsilon 4}, X_{s,\varepsilon 5}, X_{s,\varepsilon 6}, X_{s,\varepsilon 7}, X_{s,\varepsilon 8}]^T, \tag{56}$$

$$f_n = \frac{n-1}{N} f_s, \qquad n = 1, 2, ..., N, \tag{57}$$

where $x_{s,\varepsilon}^T(n)$ is the desired signal row matrix in the time domain, $x_{s,\varepsilon i}$ $(i = 1, 2, ..., 8)$ are the elements of $x_{s,\varepsilon}^T(n)$, $\varepsilon_{s,L1}$, $\varepsilon_{s,L2}$, $\varepsilon_{s,L4}$, $\varepsilon_{s,R1}$, $\varepsilon_{s,R2}$, and $\varepsilon_{s,R4}$ are the normal Y strains of the elements whose positions correspond to the strain gauges L_1, L_2, L_4, R_1, R_2, and R_4, $\varepsilon_{s,TL}$ and $\varepsilon_{s,TR}$ are the normal strains of the elements whose positions correspond to the strain rosettes L_3 and R_3 (as shown in Figs. 6 and 11), $X_{s,\varepsilon}^T(f_n)$ is the desired signal row matrix in the frequency domain, and $X_{s,\varepsilon i}$ $(i = 1, 2, ..., 8)$ are the elements of $X_{s,\varepsilon}^T(f_n)$.

According to formula (42), the following formulas can be obtained:

$$\bar{F}^T(f_n) = [H(f)]_{8 \times 8}^{-1} \cdot X_{s,\varepsilon}^T(f_n), \tag{58}$$

$$\bar{F}^T(f_n) = [\bar{F}_{Z1}, \bar{F}_{Z2}, \bar{F}_{Y1}, \bar{F}_{Y2}, \bar{F}_{X1}, \bar{F}_{X2}, \bar{M}_{Y1}, \bar{M}_{Y2}]^T, \tag{59}$$

where $\bar{F}^T(f_n)$ is the row matrix of forces and moments used to reproduce the desired strain row matrix $X_{s,\varepsilon}^T(f_n)$ in the frequency domain, $\bar{F}_{Z1}$, $\bar{F}_{Z2}$, $\bar{F}_{Y1}$, $\bar{F}_{Y2}$, $\bar{F}_{X1}$, $\bar{F}_{X2}$, $\bar{M}_{Y1}$, and $\bar{M}_{Y2}$ are the elements of $\bar{F}^T(f_n)$, and $[H(f)]_{8 \times 8}^{-1}$ is the inverse of the system frequency response function matrix $[H(f)]_{8 \times 8}$.

According to formula (51), the force and moment row matrix $[F]^T$, used to produce the desired strain row matrix $x_{s,\varepsilon}^T(n)$ in the time domain, can be obtained as follows:

$$[F]^T = \frac{1}{S_{st}(n)} IFFT\left[\frac{\bar{F}(f_n)}{(1 + A_w)e^{j\pi n}}\right], \tag{60}$$

$$[F]^T = [F_{Z1}, F_{Z2}, F_{Y1}, F_{Y2}, F_{X1}, F_{X2}, M_{Y1}, M_{Y2}]^T, \tag{61}$$

where *IFFT* represents the inverse fast Fourier transformation, F_{Z1}, F_{Z2}, F_{Y1}, F_{Y2}, F_{X1}, F_{X2}, M_{Y1}, and M_{Y2} are the elements of $[F]^T$.

As indicated in formula (58), the input loading signals in the frequency domain were obtained via the inverse of the system frequency response function matrix and the desired signals in the frequency domain. The number of accepted *FFT* points was 8192. Because the number of sampling points in each channel of the desired strain signal measured during an entire test cycle on the Hainan proving ground was 1220,608, the desired signal of each channel was divided into 298 sections, with each section having 8192 data points. In order to ensure the accuracy of calculation in the adjacent parts of the neighboring sections, they overlapped, as shown in Fig. 18, with the input loading signal points used to reproduce the desired signals calculated in one section after another, and the middle half of the obtained data points in each section connected and accepted as the input loading signal data points. The number of obtained data points for each channel of the input loading signal was also 1220,608.
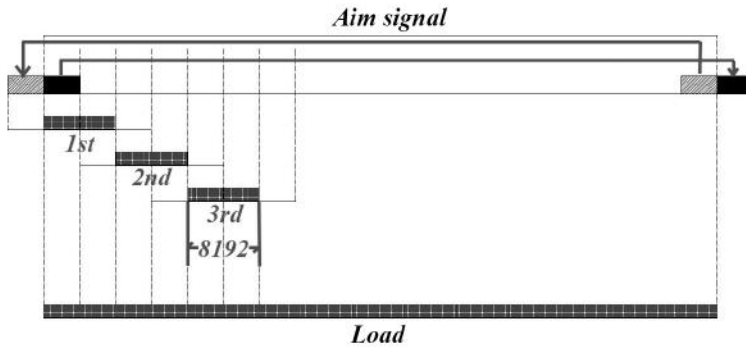

Fig. 18. Connections of the loads.

Subsequently, the input loading signal data points were applied to the dynamic finite-element model of the rear axle to reproduce the desired strain signals and the correct stress and strain distributions in the structure. Since the model is a fully linear one, an iteration process was not necessary.

Because the number of input loading data points which can be handled with the modal transient analysis module of RADIOSS is about 80,000, each channel input loading signal, comprising 1220,608 data points, was divided into 16 sections. In order to ensure the accuracy of calculation in the adjacent parts of the neighboring sections, they were overlapped by 1000 data points, so that the initial response values of the Modal transient module were always zeros. The numbers of data points in each of the 16 sections are shown in Table 6. It should be pointed out that the response data points corresponding to the preceding 1000 data points in each section, which are the last 1000 points in the last section, were discarded. The remaining response data points corresponding to the effective data points in each section were consequently connected and accepted as the achieved signal.

6. **Comparisons between the Achieved and Desired Signals**. Figure 19 shows the desired and achieved signals of the strain gauge or rosette L_1, L_2, L_3, L_4, R_1, R_2, R_3, and R_4 shown in Figs. 6 and 11. Figure 19i and j shows the zoom-in of the signals in Fig. 19g and h. The simulation error E_{rs} is defined as

$$E_{rs} = 0.8 \frac{\sum [y_d(n) - y(n)]^2}{\sum y_d^2(n)} + 0.2 \frac{\max(|y_d(n) - y(n)|)}{\max(|y_d(n)|)}, \qquad (62)$$

where $y_d(n)$ is the desired signal and $y(n)$ is the achieved signal.

T a b l e 6

**The Number of Data Points in Each Loading Signal Section**

| Section	Number of data points
No. 1	0 + 78,000
No. 2	1000 + 78,000
No. 3	1000 + 78,000
No. 4	1000 + 78,000
No. 5	1000 + 78,000
No. 6	1000 + 78,000
No. 7	1000 + 78,000
No. 8	1000 + 78,000
No. 9	1000 + 78,000
No. 10	1000 + 78,000
No. 11	1000 + 78,000
No. 12	1000 + 78,000
No. 13	1000 + 78,000
No. 14	1000 + 78,000
No. 15	1000 + 78,000
No. 16	1000 + 50,608
Number of effective data points	1220,608
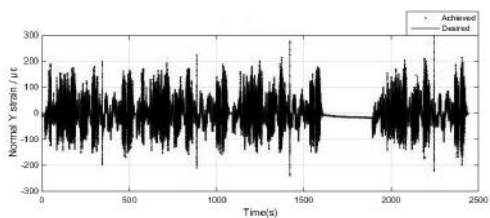
a (reproduction of L_1)
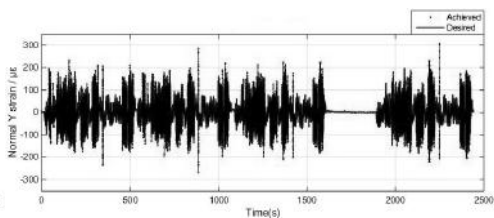
b (reproduction of R_1)
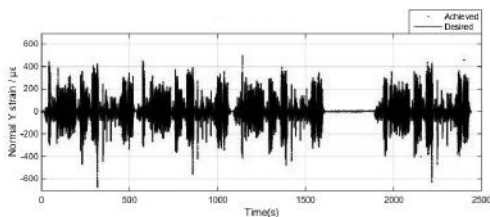
c (reproduction of L_2)
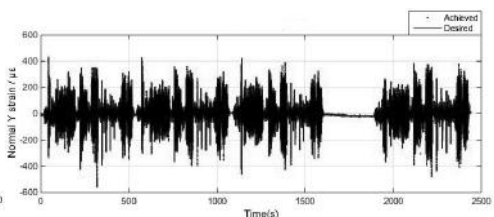
d (reproduction of R_2)
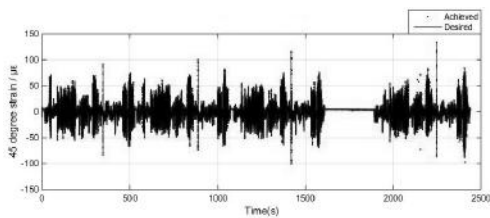
e (reproduction of L_3)
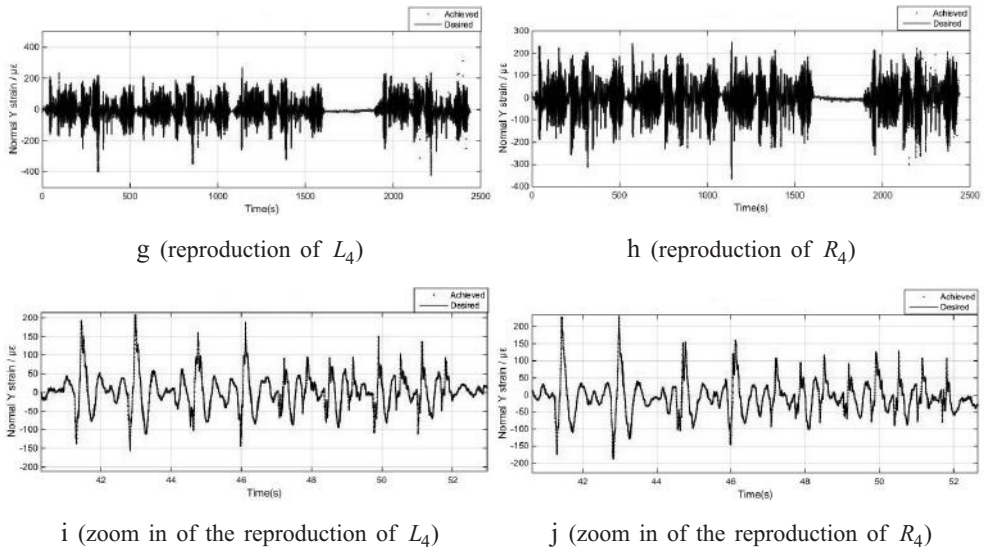

f (reproduction of R_3)

g (reproduction of L_4)

h (reproduction of R_4)

i (zoom in of the reproduction of L_4)

j (zoom in of the reproduction of R_4)
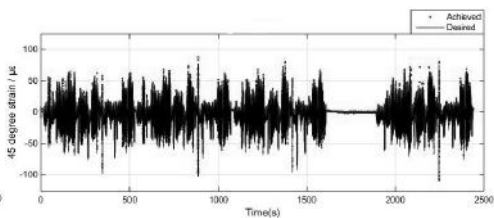
Fig. 19. Signals of strain gauge or rosette L_1, L_2, L_3, L_4, R_1, R_2, R_3, and R_4.

The simulation errors for the strain gauges or rosettes are given in Table 7, with the maximum error being 26.02% (R_3) and the minimum error 7.24% (R_1), which are small enough according to the experience gained in doing the multi-axial loading testing and acceptable. As mentioned above, the strain gauge R_5 is not a control sensor for obtaining the input loading signals but used to check if the strain distribution of the axle is correctly reproduced, whose desired and achieved signals are shown in Fig. 20, with the error being 22.58%. Figure 20b shows the zoom-in of Fig. 20a. Thus, the error is small enough, indicating that the desired signal of strain gauge R_5 and the strain distribution in the axle are correctly reproduced.

T a b l e 7
Simulation Errors for Strain Gauge or Rosette L_1, L_2, L_3, L_4, R_1, R_2, R_3, and R_4

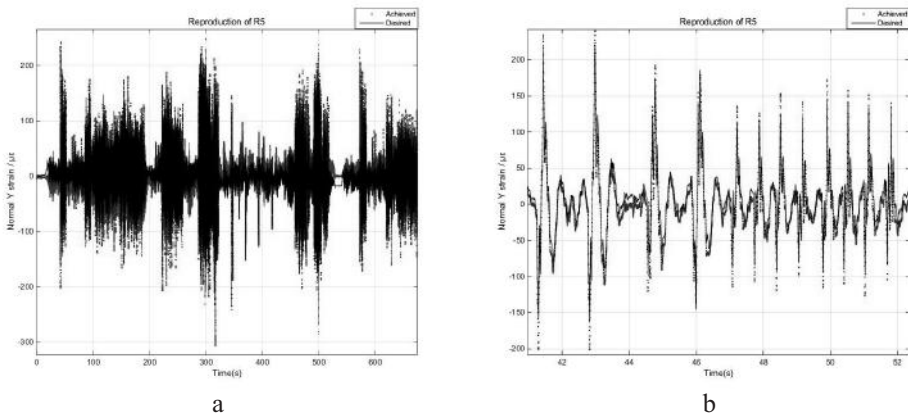|	L_1	R_1	L_2	R_2	L_3	R_3	L_4	R_4
E_{rs}	10.10%	7.24%	10.98%	10.06%	11.66%	26.02%	13.56%	15.45%

a

b

Fig. 20. Reproduction of R_5.

7. **Fatigue Life Prediction of the Rear Axle Housing**. The local strain approach [20–22] is applied to predict the fatigue life of the rear axle housing, whose basic equations are the cyclic stress–strain curve,

$$\frac{\Delta\varepsilon}{2} = \frac{\Delta\sigma}{2E} + \left(\frac{\Delta\sigma}{2K'}\right)^{1/n'}, \tag{63}$$

and the strain–life equation,

$$\frac{\Delta\varepsilon}{2} = \frac{\sigma'_f - \sigma_0}{E}(2N_f)^b + \varepsilon'_f(2N_f)^c, \tag{64}$$

where E is the cyclic elastic modulus, K' is the cyclic strength coefficient, n' is the cyclic strain hardening exponent, σ'_f is the fatigue strength coefficient, b is the fatigue strength exponent, ε'_f is the fatigue ductility coefficient, c is the fatigue ductility exponent, $\Delta\varepsilon$ is the strain range of the stress-strain hysteresis loop caused by the loading history in the material, $\Delta\sigma$ is the stress range of the loop, and σ_0 is the mean stress of the loop. $\Delta\varepsilon$, $\Delta\sigma$, and σ_0 for each stress-strain hysteresis loop in the material can be obtained by local stress–strain response analysis [22]. The housing of the axle is made with a material equivalent to 1020, a USA steel, whose fatigue properties are listed in Table 8 [23].

T a b l e 8

Fatigue Properties of 1020 Steel [23]

Order No.	Parameter	Data
1	Cyclic elastic modulus E, GPa	203
2	Cyclic strength coefficient K', MPa	1221
3	Cyclic strain hardening exponent n'	0.24
4	Fatigue strength coefficient σ'_f, MPa	895
5	Fatigue strength exponent b	-0.11
6	Fatigue ductility coefficient ε'_f	0.29
7	Fatigue ductility exponent c	-0.47

Neuber's rule is applied to predict the local stress-strain response in the critical elements from the strain histories of the elements close to the critical elements. Neuber's rule is expressed with formula (65),

$$K_f^2 \Delta\sigma_C \Delta\varepsilon_C = \Delta\sigma_A \Delta\varepsilon_A, \tag{65}$$

where $\Delta\sigma_C$ and $\Delta\varepsilon_C$ are the local stress and strain range of the hysteresis loop formed in element C whose strain signal is known, respectively, $\Delta\sigma_A$ and $\Delta\varepsilon_A$ are the local stress and strain range of the corresponding hysteresis loop in element A (critical element), respectively, and K_f is the fatigue notch factor.

Neuber's rule can also be expressed with formula (66),

$$K_f^2 \Delta S_C \Delta e_c = K_f^2 E \Delta e_C^2 = K_f^2 \frac{\Delta S_C^2}{E} = \Delta\sigma_A \Delta\varepsilon_A, \tag{66}$$

where ΔS_C and Δe_C are the nominal stress and strain range of element C, respectively, which are obtained by processing the calculated nominal stress signal with the rainflow counting arithmetic. Because the nominal stress signals of each element can be obtained with the dynamic finite element analysis model above, formula (66) is more useful in predicting the fatigue life of each element of the finite element model, with $A = C$ and $K_f = 1$, which implies that the nominal stress signal of each element is used to predict its fatigue life and the stress concentration effect has been taken into account in the finite element analysis.

A software based on the local stress-strain approach [22] has been made to process the strain histories and to predict the fatigue lives and damages caused by them. Tables 9 and 10 show the fatigue life prediction results of the calculated and measured strain histories of the strain gauges L_1, L_2, L_3, L_4, R_1, R_2, R_3, and R_4, as shown in Fig. 11, with formula (65) and $K_f = 1$ applied in the life predictions. Let D_c and D_m be the predicted fatigue damages caused in a whole Hainan driving cycle with the calculated and measured strain signal, respectively. The corresponding predicted fatigue lives are

$$L_c = \frac{1}{D_c}, \tag{67}$$

$$L_m = \frac{1}{D_m}. \tag{68}$$

The error *Err* is defined as

$$Err = \left| \frac{L_c - L_m}{L_m} \right| \times 100\%, \tag{69}$$

where L_c and L_m are the predicted fatigue lives or the numbers of the whole Hainan driving cycles the component can experience before the fatigue failure occurs.

T a b l e 9

Fatigue Life Prediction Results of the Calculated and Measured Strain Histories of the Strain Gauges L_1, L_2, L_3, and L_4

Strain signal		L_1	L_2	L_3	L_4
Measured	Max. strain/$\mu\varepsilon$	298.08	491.78	134.77	262.07
	Min. strain/$\mu\varepsilon$	-238.32	-672.78	-100.37	-417.22
	D_m	5.746e–11	4.002e–8	2.527e–14	3.040e–10
	L_m/Hainan drive cycle	1.740e+10	2.499e+7	3.957e+13	3.290e+9
Calculated	Max. strain/$\mu\varepsilon$	297.05	498.65	133.90	263.02
	Min. strain/$\mu\varepsilon$	-238.30	-672.44	-100.46	-417.77
	D_c	5.718e–11	4.124e–8	2.590e–14	3.234e–10
	L_c/Hainan drive cycle	1.749e+10	2.425e+7	3.860e+13	3.092e+9
Err		0.52%	2.96%	2.45%	6.02%

T a b l e 1 0

Fatigue Life Prediction Results of the Simulation and Measured Strain Histories of the Strain Gauges R_1, R_2, R_3, and R_4

Stain signal		R_1	R_2	R_3	R_4
Measured	Max. strain/$\mu\varepsilon$	306.69	430.65	77.00	246.50
	Min. strain/$\mu\varepsilon$	−267.45	−557.47	−110.6	−364.30
	D_m	1.182e–10	1.776e–8	4.791e–15	1.774e–10
	L_m/Hainan drive cycle	8.459e+9	5.630e+7	2.087e+14	5.640e+9
Calculated	Max.strain/$\mu\varepsilon$	307.98	431.03	88.05	247.24
	Min.strain/$\mu\varepsilon$	−267.49	−557.44	−107.42	−364.53
	D_c	1.184e–10	1.791e–8	5.285e–15	1.883e–10
	L_c/Hainan drive cycle	8.445e+9	5.583e+7	1.892e+14	5.310e+9
Err		0.17%	0.34%	9.34%	5.85%

As shown in Tables 9 and 10, the predicted life errors between the calculated and measured strain histories of strain gauge L_1, L_2, L_3, L_4, R_1, R_2, R_3, and R_4 are between 0.17 and 9.34%, which are quite small, indicating that the accuracy of the simulation is quite high. Thus, the forces and moments obtained above for reproducing the desired strain response signals can be used for fatigue simulation.

Conclusions. The spindle coupled multi-axial loading rig test of the rear axle is comparatively accurately simulated with the method presented, with the simulation errors between 7.24 and 26.02% which are small enough according to the experience gained in doing the multi-axial loading testing and acceptable. The method focuses on accurately reproducing the strain distribution in the selected specimen experienced in the fields, with which the problems with constructing the complicated whole vehicle finite element model including the tire model and too short time duration which can be simulated are avoided. Each channel desired signal adopted has 1,220,608 data points and a duration of 2441.216 s, which is measured in a whole test cycle on Hainan proving ground according to the specifications of durability test of SAIC GM Wuling Automobile Co., Ltd. In fact, the number of the data points or the time duration of the desired signal which can be simulated with the method is not limited. Thus, the method presented is practical and efficient.

Р е з ю м е

Запропоновано практичний метод моделювання багатовісного циклічного навантаження задньої вісі автомобіля з урахуванням взаємодії різних чинників. Розроблено динамічну скінченноелементну модель задньої вісі та виконано її верифікацію за допомогою калібрувальних тестів при статичному навантаженні. Із використанням випробувальної системи Schenck ITFC моделюється процес, який включає ідентифікацію системи, обчислення вхідних сигналів навантаження для скінченноелементної моделі, вихідних сигналів напружень та деформації, а також порівняння розрахункових сигналів із реальними. За допомогою програмного забезпечення Matlab реалізовано програми обробки даних, що легко відтворюються. Проведено вимірювання динамічних сигналів напружень протягом 2441,216 с навантаження на автомобіль-

ному стенді Hainan за допомогою тензодатчиків, розміщених у ключових точках задньої вісі автомобіля. Отримано задовільний збіг розрахункового розподілу деформації у задній вісі автомобіля з експериментальним.

1. G. Jacoby, Betriebslasten Simulation an Fahrzeugbauteilen Mittels servohydraulischer Prufeinrichtungen, *VDI Berichte*, **632**, 1–54 (1987).

2. K. J. White, "The road simulator – a practical laboratory approach," in: *Prediction and Simulation of In-Service Conditions*, IMechE Conference Publications 1985-5, Institute of Mechanical Engineers, London (1985), pp. 69–80.

3. K. Feitzelmayer and U. Breitling, "Development of commercial vehicle rear driven axles on multi-axis test set-ups," in: *Prediction and Simulation of In-Service Conditions*, IMechE Conference Publications 1985-5, Institute of Mechanical Engineers, London (1985), pp. 131–138.

4. C. J. Dodds, *A Computer System for Multi-Channel Remote Parameter Control of a Test Specimen*, MTS publication (1977).

5. X. Wang, *Fundamentals of Automotive Reliability Engineering* [in Chinese], Tsinghua University Press, Beijing (2007).

6. *Simulation Testing and SPiDAR-IDC*, Fairhurst Structural Monitoring publication (1987).

7. J. De Cuyper, D. Coppens, C. Liefooghe, and J. Debille, "Advanced system identification methods for improved service load simulation on multi-axial test rigs," *Eur. J. Mech. Environ. Eng. M*, **44**, No. 1, 27–39 (1999).

8. J. De Cuyper and D. Coppens, "Service load simulation on multi-axis test rigs," *Sound Vib.*, **30**, No. 1, 30–35 (1999).

9. S. You and S. Joo, *Virtual Testing and Correlation with Spindle Coupled Full Vehicle Testing System*, SAE Technical Paper 2006-01-0993 (2006).

10. R. E. Canfield and M. A. Villaire, T*he Development of Accelerated Component Durability Test Cycles Using Fatigue Sensitive Editing Techniques*, SAE Technical Paper 920660 (1992).

11. K. J. Dittmann, F. J. Albright, and C. Leser, "Validation of virtual prototypes via a virtual test laboratory," in: Proc. of the 17th European MSC.ADAMS User Conference (November 13–14 2002, London, UK).

12. S. You, C. Leser, and E. Young, *Tools for Integration of Analysis and Testing*, SAE Technical Paper 2003-01-1606 (2003).

13. B. P. Naganarayana, S. Shankar, V. S. Bhattachar, et al., *N-Hance; Software for Identification of Critical BSR Location in Automotive Assemblies Using Finite Element Models*, SAE Technical Paper 2003-01-1522 (2003).

14. R. K. Hodkin, "Hydraulic vibrators in automobile testing with special reference to the rootes suspension parameter rig," *Proc. Inst. Mech. Eng.*, **182**, No. 254–62 (1967).

15. S. S. You and D. Fricke, "Advances of virtual testing and hybrid simulation in automotive performance and durability evaluation," *SAE Int. J. Mater. Manuf.*, **4**, No. 1, 98–110 (2011), DOI: 10.4271/2011-01-0029.

16. G. Choi, H. Min, and S. Paik, *Dynamic Stress Analysis of Vehicle Using Virtual Proving Ground Approach*, SAE Technical Paper 2000-01-0121 (2000).

17. R. Edara, S. Shih, N. Tamini, et al., *Heavy Vehicle Suspension Frame Durability Analysis Using Virtual Proving Ground*, SAE Technical Paper 2005-01-3609 (2005).

18. D. Kim and S. Joo, *Generation of 3-D Virtual Block Belgian Road for Prediction of Road Load*, SAE Technical Paper 2011-28-0077 (2011).

19. Y. Zhang, T. Stawiarski, M. Subramanian, et al., *Full Vehicle Finite Element Model 4-Post Durability Analysis*, SAE Technical Paper 2005-01-1402 (2005).

20. N. Dowling, *A Discussion of Methods for Estimating Fatigue Life*, SAE Technical Paper 820691 (1982).

21. H. S. Reemsnyder, *Constant Amplitude Fatigue Life Assessment Models*, SAE Technical Paper 820688 (1982).

22. D. Socie, *Variable Amplitude Fatigue Life Estimation Models*, SAE Technical Paper 820689 (1982).

23. B. Boardman, *Crack Initiation Fatigue – Data, Analysis, Trends and Estimation*, SAE Technical Paper 820682 (1982).